Available online at www.sciencedirect.com
ScienceDirect
Journal of Power Sources 173 (2007) 210–221
JOURNAL OF POWER SOURCES
www.elsevier.com/locate/jpowsour

# Novel serpentine-baffle flow field design for proton exchange membrane fuel cells

Wang Xiao-Dong [a], Duan Yuan-Yuan [b], Yan Wei-Mon [c,*]

[a] *Department of Thermal Engineering, School of Mechanical Engineering, University of Science & Technology Beijing, Beijing 100083, China*
[b] *Key Laboratory for Thermal Science and Power Engineering of Ministry of Education, Tsinghua University, Beijing 100084, China*
[c] *Department of Mechatronic Engineering, Huafan University, Taipei 22305, Taiwan*

Received 13 July 2007; received in revised form 11 August 2007; accepted 13 August 2007
Available online 21 August 2007

**Abstract**

An appropriate flow field in the bipolar plates of a fuel cell can effectively enhance the reactant transport rates and liquid water removal efficiency, improving cell performance. This paper proposes a novel serpentine-baffle flow field (SBFF) design to improve the cell performance compared to that for a conventional serpentine flow field (SFF). A three-dimensional model is used to analyze the reactant and product transport and the electrochemical reactions in the cell. The results show that at high operating voltages, the conventional design and the baffled design have the same performance, because the electrochemical rate is low and only a small amount of oxygen is consumed, so the oxygen transport rates for both designs are sufficient to maintain the reaction rates. However, at low operating voltages, the baffled design shows better performance than the conventional design. Analyses of the local transport phenomena in the cell indicate that the baffled design induces larger pressure differences between adjacent flow channels over the entire electrode surface than does the conventional design, enhancing under-rib convection through the electrode porous layer. The under-rib convection increases the mass transport rates of the reactants and products to and from the catalyst layer and reduces the amount of liquid water trapped in the porous electrode. The baffled design increases the limiting current density and improves the cell performance relative to conventional design.


*Keywords:* Proton exchange membrane fuel cell; Serpentine flow field; Electrochemical reaction; Baffle

## 1. Introduction

Fuel cells are electrochemical reactors now used for a wide variety of applications. Due to their high efficiency (nearly twice that of the present generation of internal combustion engines), portability and near-zero emissions, fuel cells are attractive as a power source for automobiles. Of the various types of fuel cells, the proton exchange membrane fuel cell (PEMFC) operates at near-room temperatures and is considered to be a good choice for automotive applications. However, the commercialization of the PEMFC is still hindered by several technological problems, among which is severe water flooding of the cathode and the resulting mass transport losses [1–3]. Over recent decades, in an effort to improve PEMFC performance, many analyses, models and numerical simulations have been developed [1–20] for various transport phenomena and electrochemical kinetics to gain a better understanding and to develop strategies for optimal design and operation scenarios.

The flow field design in the bipolar plates is one of the most important issues in a PEMFC. An appropriate flow field design in the bipolar plates can improve the reactant transport and the efficiency of the thermal and water management. To this end, different flow field configurations, including parallel, serpentine, interdigitated, and many other combined versions, have been developed. Many efforts have been devoted to the optimal flow field design to improve cell performance [14–33].

Nguyen [24] first proposed the interdigitated flow field, in which baffles were added at the ends of some channels. The baffle design forced the reactants to flow through the gas diffusion layer (GDL) and the shear force of this reactants flow helped blow out the liquid water trapped in the inner layers of the electrodes. As a result, the mass transport rates of

* Corresponding author. Tel.: +886 2 2663 2102; fax: +886 2 2663 1119.
*E-mail address:* wmyan@huafan.hfu.edu.tw (W.-M. Yan).

0378-7753/$ – see front matter © 2007 Elsevier B.V. All rights reserved.
doi:10.1016/j.jpowsour.2007.08.037

**Nomenclature**

| | |
|---|---|
| $a$ | chemical activity of water vapor |
| $A_{cha}$ | cathode cross-sectional inlet flow area ($m^2$) |
| $Aj_0^{ref}$ | reference exchange current density ($A\,m^{-3}$) |
| $A_{total}$ | reaction area ($m^2$) |
| $b$ | source term of variable $\phi$ |
| $C$ | mass fraction |
| $C_F$ | quadratic drag factor |
| $d$ | hydraulic diameter of the flow channel (m) |
| $D$ | mass diffusivity ($m^2\,s^{-1}$) |
| $F$ | Faraday constant (96,487 $C\,mol^{-1}$) |
| $I$ | current density ($A\,m^{-2}$) |
| $j$ | current density ($A\,m^{-3}$) |
| $k_c$ | coefficient of water vapor condensation rate ($s^{-1}$) |
| $k_e$ | coefficient of water vapor evaporation rate ($s^{-1}$) |
| $k_p$ | permeability ($m^2$) |
| $L$ | distance along the channel measured form the inlet (m) |
| $M$ | molecular weight ($kg\,mol^{-1}$) |
| $P$ | pressure (atm) |
| $Q$ | mass flow rate ($kg\,s^{-1}\,m^{-2}$) |
| $R$ | universal gas constant (8.314 $J\,mol^{-1}\,K^{-1}$) |
| $s$ | volume ratio occupied by liquid water |
| $t$ | time (s) |
| $T$ | temperature (K) |
| $u$ | $X$-direction velocity ($m\,s^{-1}$) |
| $v$ | $Y$-direction velocity ($m\,s^{-1}$) |
| $V$ | fuel velocity at the cathode inlet ($m\,s^{-1}$) |
| $w$ | $Z$-direction velocity ($m\,s^{-1}$) |
| $W_P$ | cathode pressure drop loss ($W\,m^{-2}$) |
| $W_r$ | width of rib (m) |
| $x$ | $X$-direction coordinate (m) |
| $y$ | $Y$-direction coordinate (m) |
| $z$ | $Z$-direction coordinates (m) |
| $Z_f$ | species valence |

*Greek letters*

| | |
|---|---|
| $\alpha_a$ | electrical transfer coefficient in forward reaction |
| $\alpha_c$ | electrical transfer coefficient in backward reaction |
| $\varepsilon$ | porosity |
| $\eta$ | overpotential (V) |
| $\lambda$ | water content in membrane |
| $\mu$ | viscosity (Pa s) |
| $\nu$ | kinematic viscosity ($m^2\,s^{-1}$) |
| $\Xi_\phi$ | exchange coefficient |
| $\rho$ | density ($kg\,m^{-3}$) |
| $\sigma_m$ | electric conductivity of membrane |
| $\tau$ | tortuosity of the pores in the porous medium |
| $\phi$ | dependent variables |
| $\Phi$ | phase potential function (V) |

*superscripts*

| | |
|---|---|
| ref | reference value |

*subscripts*

| | |
|---|---|
| a | anode |
| aver | average |
| c | cathode |
| eff | effective |
| in | inlet |
| $k$ | $k$th species of the mixture |
| $H^+$ | hydrogen ion |
| $H_2$ | hydrogen |
| $H_2O$ | water |
| $O_2$ | oxygen |
| sat | saturation |
| total | total |

the reactants from the flow channel to the inner catalyst layer were improved and the water flooding problem at the cathode was significantly reduced. Soong et al. [31] proposed a novel flow channel configuration in which the baffles were inserted transversely in the channel of a conventional parallel flow field to form a partially blocked fuel channel. They found that reducing the gap size and/or increasing the number of baffles enhanced the reactant transport and cell performance. Liu et al. [32] investigated the effect of baffle-blocked channels on the reactant transport and cell performance of PEMFC with a conventional parallel flow field. Their results indicated that the baffles forced more reactants from the flow channel into the GDL to enhance the chemical reactions which augmented the cell performance.

These investigations have shown that enhancing the convection of reactants through the GDL by adding baffles is an effective way to reduce water flooding at the cathode and increase the reactant mass transport, thus improving both the cell performance and the operating stability. Based on this understanding, the effects of three new serpentine-baffle flow field designs for the PEMFC were investigated in this study. The flows were obtained by inserting the baffles in different locations in the channels for a conventional serpentine flow field. A three-dimensional numerical model was used to compare the cell performance for baffled and conventional designs. The effects of liquid water formation on the reactant transport were taken into account in the model. The oxygen mass flow rates and the liquid water distributions at the interface between the cathode GDL and the catalyst layer (CL), and local current densities for baffled and conventional designs are analyzed to show the advantages of the baffled design. The compressor powers for baffled and conventional designs are also evaluated.

## 2. Flow field design

Water flooding normally occurs at the cathode electrode of the PEMFC because the electrochemical reaction on the cathode produces water vapor. If the partial pressure of the water vapor is higher than the saturation pressure, water vapor condenses to

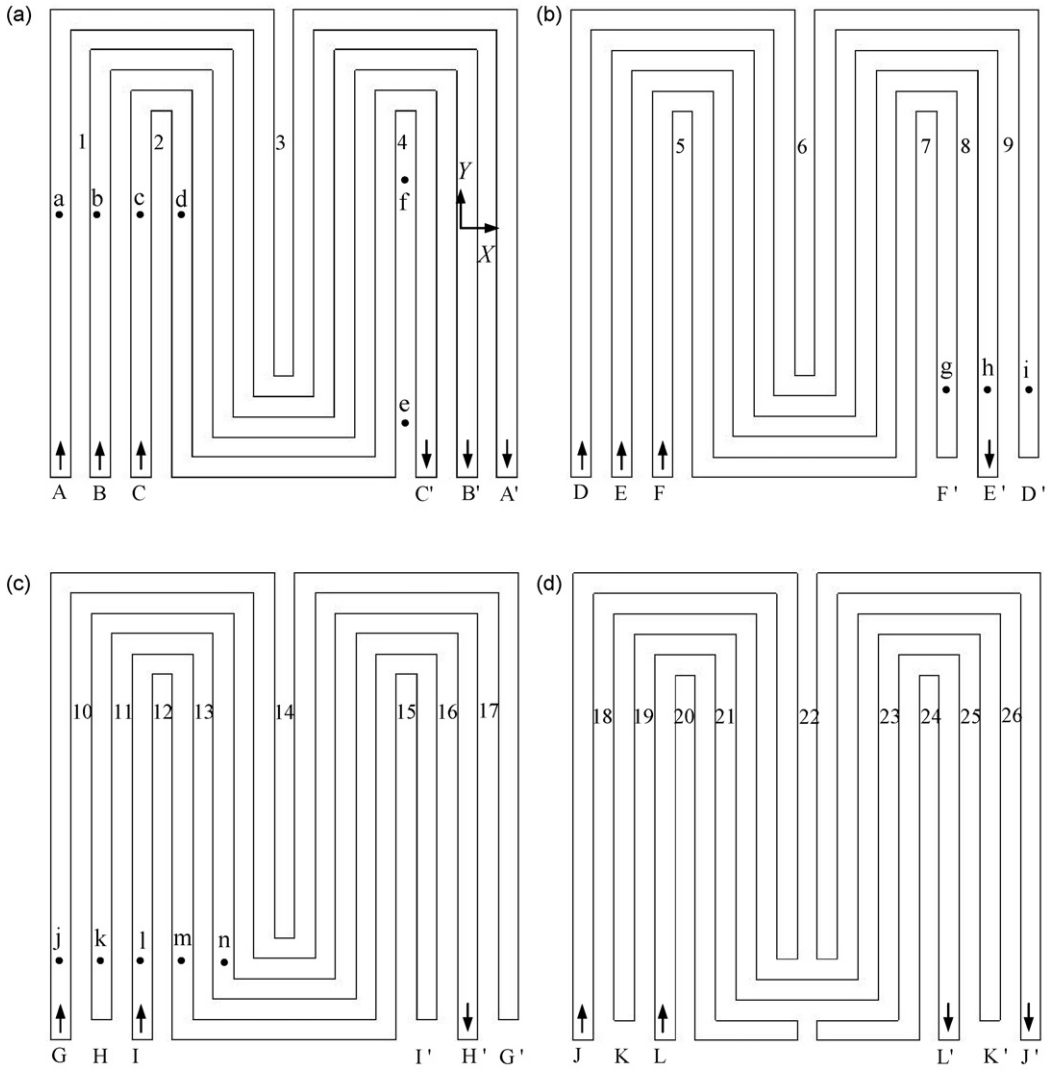


Fig. 1. Cathode flow fields designs. (a) SFF; (b) SBFF-1; (c) SBFF-2; and (d) SBFF-3.

form liquid water. When a large amount of liquid water accumulates in the porous layer pores, the oxygen transport resistance increases and the oxygen mass flow rate decreases. Therefore, the cathode flow field design is a key factor for enhancing reactant and product transport and for removing the liquid water. The present paper analyzes various cathode flow field designs. The results are compared to a triple serpentine flow field to identify the advantages of the novel baffled design.

Fig. 1 compares the cathode flow fields for the conventional and baffled designs. Fig. 1(a) shows a conventional triple serpentine flow field, which includes three serpentine loops, AA′, BB′, and CC′. The reactants enter the cell from the inlets of the three loops and then flow along the channels. Some of the reactants diffuse into the GDL and CL and are consumed by the electrochemical reactions, while the remainder flows out of the cell from the outlets of the three loops. Fig. 1(b)–(d) shows three triple serpentine-baffle flow field designs, named SBFF-1, SBFF-2, and SBFF-3. The SBFF-1 includes three serpentine loops, DD′, EE′, and FF′, with the same inlet configuration as the conventional design, but with two baffles added at the outlets of DD′ and FF′. Therefore, the reactants only flow out of the cell from the outlet of EE′. The SBFF-2 design has three serpentine loops, GG′, HH′, and II′, with three baffles added at the inlet of HH′, and at the outlets of GG′ and II′. The SBFF-3 design also has three serpentine loops, JJ′, KK′, and LL′, with two baffles added at the inlet and outlet of KK′, and another two baffles placed at the center of JJ′ and LL′ as shown in Fig. 1(d). The anodes for all four cell designs are parallel flow field designs with 12 flow channels and 11 ribs.

This paper considered miniature fuel cells with dimensions of 23 mm × 23 mm × 2.845 mm. All four designs had the same 23 mm × 23 mm reaction area dimensions, and the same GDL, CL, and membrane thicknesses. The detailed physical dimensions of the fuel cells are summarized in Table 1. The operating conditions were all the same for a fair comparison for all the cells. The fuel cell temperature was assumed to be 323 K, the reactants on the anode side included hydrogen and water vapor with a relative humidity of 100%, the reactants on the cathode side contained oxygen, nitrogen, and water vapor with a relative humidity of 100%, the inlet flow rate on the anode side

Table 1
Fuel cell dimensions

| Quantity | Value |
|---|---|
| Reaction area ($mm^2$) | $23 \times 23$ |
| Channel width (mm) | 1 |
| Rib width (mm) | 1 |
| Channel height (mm) | 1 |
| Rib height (mm) | 1 |
| Anode GDL thickness (mm) | 0.4 |
| Anode CL thickness (mm) | 0.005 |
| Membrane thickness (mm) | 0.035 |
| Cathode GDL thickness (mm) | 0.005 |
| Cathode CL thickness (mm) | 0.4 |

was 260 $cm^3\,min^{-1}$, the inlet flow rate on the cathode side was 700 $cm^3\,min^{-1}$.

## 3. Model

A three-dimensional model of the full fuel cell was used to analyze the electrochemical reactions and transport phenomena of the reactants and products. The cell was divided into the anode flow channels, membrane electrode assembly (MEA, including the anode GDL, anode CL, proton exchange membrane, cathode CL, and cathode GDL), and cathode flow channels. The governing equations included the mass, momentum, species, and electrical potential conservation equations. The model assumed that the system is three-dimensional and steady, the inlet reactants are ideal gases, the system is isothermal, the flow is laminar, the fluid is incompressible, the thermophysical properties are constant, and the porous GDL, CL, and proton exchange membrane (PEM) layers are isotropic.

The transport equations for the three-dimensional PEMFCs are given as

Continuum equation:

$$\frac{\partial u}{\partial x} + \frac{\partial v}{\partial y} + \frac{\partial w}{\partial z} = 0 \tag{1}$$

Momentum equation:

$$\varepsilon_{\text{eff}}\left(u\frac{\partial u}{\partial x} + v\frac{\partial u}{\partial y} + w\frac{\partial u}{\partial z}\right) = -\frac{\varepsilon_{\text{eff}}}{\rho}\frac{\partial P}{\partial x} + \nu\varepsilon_{\text{eff}}\left(\frac{\partial^2 u}{\partial x^2} + \frac{\partial^2 u}{\partial y^2} + \frac{\partial^2 u}{\partial z^2}\right) + S_u \tag{2}$$

$$\varepsilon_{\text{eff}}\left(u\frac{\partial v}{\partial x} + v\frac{\partial v}{\partial y} + w\frac{\partial v}{\partial z}\right) = -\frac{\varepsilon_{\text{eff}}}{\rho}\frac{\partial P}{\partial y} + \nu\varepsilon_{\text{eff}}\left(\frac{\partial^2 v}{\partial x^2} + \frac{\partial^2 v}{\partial y^2} + \frac{\partial^2 v}{\partial z^2}\right) + S_v \tag{3}$$

$$\varepsilon_{\text{eff}}\left(u\frac{\partial w}{\partial x} + v\frac{\partial w}{\partial y} + w\frac{\partial w}{\partial z}\right) = -\frac{\varepsilon_{\text{eff}}}{\rho}\frac{\partial P}{\partial z} + \nu\varepsilon_{\text{eff}}\left(\frac{\partial^2 w}{\partial x^2} + \frac{\partial^2 w}{\partial y^2} + \frac{\partial^2 w}{\partial z^2}\right) + S_w \tag{4}$$

Species equation:

$$\varepsilon_{\text{eff}}\left(u\frac{\partial C_k}{\partial x} + v\frac{\partial C_k}{\partial y} + w\frac{\partial C_k}{\partial z}\right) = D_{k,\text{eff}}\left(\frac{\partial^2 C_k}{\partial x^2} + \frac{\partial^2 C_k}{\partial y^2} + \frac{\partial^2 C_k}{\partial z^2}\right) + S_c + S_L \tag{5}$$

In the momentum equation, $\varepsilon$ is the porosity and $S_u$, $S_v$, and $S_w$ the corrected terms of the reactant flow in the gas diffusion layer and the catalyst layer and of the proton transfer in the PEM, which is listed in Table 2. In the species equation, $D_{k,\text{eff}}$ is the effective diffusion coefficient and $S_c$ represents the source terms due to the chemical reaction in the catalyst layer and the proton exchange membrane. The Bruggeman correction [34] is employed to describe the influence of the porosity on the diffusion coefficient:

$$D_{k,\text{eff}} = D_k\varepsilon^{\tau} \tag{6}$$

If the partial pressure of water vapor is greater than the saturation pressure, the liquid water forms in the PEMFC. To consider the effect of the liquid water formation, it is assumed that the pore in the porous material is blocked by liquid water, which results in the modification of the diffusion coefficient and the porosity in the species equation. The source term $S_L$ in the species equation due to the liquid water is determined by [35]

$$S_L = \begin{cases} M_{H_2O}k_c\dfrac{\varepsilon_{\text{eff}}C_{H_2O}}{\rho RT}(P_{H_2O} - P_{\text{sat}}), & \text{if } P_{H_2O} > P_{\text{sat}} \\ k_e\varepsilon_{\text{eff}}s(P_{\text{sat}} - P_{H_2O}), & \text{if } P_{H_2O} < P_{\text{sat}} \end{cases} \tag{7}$$

where the saturation $s$ is the ratio of the liquid water volume to pore volume in the porous material, $M$ the molecular weight of water, $k_c$ the condensation rate constant of water, $k_e$ the evaporation rate constant of water, and $\varepsilon_{\text{eff}}$ is the modified effective porosity of the porous medium by considering the liquid water effect which is given by

$$\varepsilon_{\text{eff}} = \varepsilon(1 - s) \tag{8}$$

The saturation pressure of water can be expressed as

$$P_{\text{sat}} = 10^{-2.1794+0.02953T-9.1837\times10^{-5}T^2+1.4454\times10^{-7}T^3} \tag{9}$$

To calculate the local current density, the phase potential equations should be solved

$$\frac{\partial}{\partial x}\left(\sigma_m\frac{\partial \Phi}{\partial x}\right) + \frac{\partial}{\partial y}\left(\sigma_m\frac{\partial \Phi}{\partial y}\right) + \frac{\partial}{\partial z}\left(\sigma_m\frac{\partial \Phi}{\partial z}\right) = S_j \tag{10}$$

where $S_j = 0$ in the membrane, $S_j = -j_a$ in the anode catalyst layer, $S_j = j_c$ in the cathode catalyst layer, $\Phi$ the phase potential, and $\sigma_m$ is the ionic conductivity of the membrane. In this study, Butler–Volmer equation [36] is used to calculate the transfer current density generated by the electrochemical reaction:

$$j_a = Aj_{0,a}^{\text{ref}}\left(\frac{C_{H_2}}{C_{H_2}^{\text{ref}}}\right)\left[e^{(\alpha_a F/RT)\eta} - \frac{1}{e^{(\alpha_c F/RT)\eta}}\right] \tag{11}$$

$$j_c = Aj_{0,c}^{\text{ref}}\left(\frac{C_{O_2}}{C_{O_2}^{\text{ref}}}\right)\left[e^{(\alpha_a F/RT)\eta} - \frac{1}{e^{(\alpha_c F/RT)\eta}}\right] \tag{12}$$

Table 2
Source terms in the governing equations

| | $S_u$ | $S_v$ | $S_w$ | $S_c$ |
|---|---|---|---|---|
| Channel | 0 | 0 | 0 | – |
| GDL | $-\frac{\nu\varepsilon_{\text{eff}}^2}{k_{\text{p}}}u - \frac{\varepsilon_{\text{eff}}^3 C_{\text{F}}\rho u}{\sqrt{k_{\text{p}}}}\sqrt{u^2+v^2+w^2}$ | $-\frac{\nu\varepsilon_{\text{eff}}^2}{k_{\text{p}}}v - \frac{\varepsilon_{\text{eff}}^3 C_{\text{F}}\rho v}{\sqrt{k_{\text{p}}}}\sqrt{u^2+v^2+w^2}$ | $-\frac{\nu\varepsilon_{\text{eff}}^2}{k_{\text{p}}}w - \frac{\varepsilon_{\text{eff}}^3 C_{\text{F}}\rho w}{\sqrt{k_{\text{p}}}}\sqrt{u^2+v^2+w^2}$ | 0 |
| | | | | $\text{H}_2 : -\frac{1}{2\text{FC}_{\text{total,a}}} j_{\text{a}}$ |
| | | | | $\text{O}_2 : -\frac{1}{4\text{FC}_{\text{total,c}}} j_{\text{c}}$ |
| | | | | $\text{H}_2\text{O} : \frac{1}{2\text{FC}_{\text{total,c}}} j_{\text{c}}$ |
| CL | $-\frac{\nu\varepsilon_{\text{eff}}^2}{k_{\text{p}}}u - \frac{\varepsilon_{\text{eff}}^3 C_{\text{F}}\rho u}{\sqrt{k_{\text{p}}}}\sqrt{u^2+v^2+w^2}$ | $-\frac{\nu\varepsilon_{\text{eff}}^2}{k_{\text{p}}}v - \frac{\varepsilon_{\text{eff}}^3 C_{\text{F}}\rho v}{\sqrt{k_{\text{p}}}}\sqrt{u^2+v^2+w^2}$ | $-\frac{\nu\varepsilon_{\text{eff}}^2}{k_{\text{p}}}w - \frac{\varepsilon_{\text{eff}}^3 C_{\text{F}}\rho w}{\sqrt{k_{\text{p}}}}\sqrt{u^2+v^2+w^2}$ | $\frac{ZF}{RT} D_{k,\text{eff},\text{H}^+} \text{C}_{\text{H}^+} \left(\frac{\partial^2\Phi}{\partial x^2} + \frac{\partial^2\Phi}{\partial y^2} + \frac{\partial^2\Phi}{\partial z^2}\right)$ |
| Membrane | $-\frac{\nu\varepsilon_{\text{eff}}^2}{k_{\text{p}}}u - \frac{\varepsilon_{\text{eff}}^3 C_{\text{F}}\rho u}{\sqrt{k_{\text{p}}}}\sqrt{u^2+v^2+w^2} + \frac{k_{\text{p}}}{\nu} Z_{\text{f}} C_{\text{H}^+} F\nabla\Phi u_x$ | $-\frac{\nu\varepsilon_{\text{eff}}^2}{k_{\text{p}}}v - \frac{\varepsilon_{\text{eff}}^3 C_{\text{F}}\rho v}{\sqrt{k_{\text{p}}}}\sqrt{u^2+v^2+w^2} + \frac{k_{\text{p}}}{\nu} Z_{\text{f}} C_{\text{H}^+} F\nabla\Phi v_y$ | $-\frac{\nu\varepsilon_{\text{eff}}^2}{k_{\text{p}}}w - \frac{\varepsilon_{\text{eff}}^3 C_{\text{F}}\rho w}{\sqrt{k_{\text{p}}}}\sqrt{u^2+v^2+w^2} + \frac{k_{\text{p}}}{\nu} Z_{\text{f}} C_{\text{H}^+} F\nabla\Phi w_z$ | |

where $Aj_0^{\text{ref}}$ is the reference exchange current density, $\alpha_{\text{a}}$ and $\alpha_{\text{c}}$ the transfer coefficient in anode and cathode catalyst layers, $\eta$ the overpotential, $R$ the gas constant, and $T$ is the temperature of the fuel cell. The ionic conductivity of the membrane can be calculated by [37]

$$\sigma_{\text{m}}(T) = \sigma_{\text{m}}^{\text{ref}} \exp\left[1268\left(\frac{1}{303} - \frac{1}{T}\right)\right] \tag{13}$$

and the reference ionic conductivity is

$$\sigma_{\text{m}}^{\text{ref}} = 0.005139\lambda - 0.00326 \tag{14}$$

$$\lambda = \begin{cases} 0.043 + 17.81a - 39.85a^2 + 36.0a^3 & 0 \le a \le 1 \\ 14 + 1.4(a-1) & 1 < a \le 3 \end{cases} \tag{15}$$

where $a$ is the activity of water vapor at the cathode side. The relationship between the phase potential and the current density is given by

$$i_x = -\sigma_{\text{m}}\frac{\partial\Phi}{\partial x} \tag{16}$$

$$i_y = -\sigma_{\text{m}}\frac{\partial\Phi}{\partial y} \tag{17}$$

$$i_z = -\sigma_{\text{m}}\frac{\partial\Phi}{\partial y} \tag{18}$$

Boundary conditions at the anode flow channels and the cathode flow channels are as follows: the inlet flow rates are constant, the inlet gas compositions are constant, and the flows are fully developed at the outlets of the anode and cathode flow channels. At the solid walls, no slip and zero fluxes are hold. At the interfaces between the gas channels, the diffuser layers, the catalyst layers, and the PEM, equalities of the velocity, mass fraction, momentum flux, and mass flux are applied. More details were given elsewhere [30–33]. All parameters used in the model are listed in Table 3.

Since these equations for this complex convection–diffusion problem cannot be solved analytically, it was solved using the finite volume method on a collocated cell-centered grid. The

Table 3
Parameters of the fuel cell

| Parameter | Value |
|---|---|
| $Aj_{0,\text{a}}^{\text{ref}}$ | $9 \times 10^8$ |
| $Aj_{0,\text{c}}^{\text{ref}}$ | $1.5 \times 10^2$ |
| $\alpha_{\text{a}}$ | 0.5 |
| $\alpha_{\text{c}}$ | 1.5 |
| $\varepsilon_{\text{channel}}$ | 1 |
| $\tau_{\text{channel}}$ | 1 |
| $k_{\text{channel}}$ | $\infty$ |
| $\varepsilon_{\text{GDL}}$ | 0.5 |
| $\tau_{\text{GDL}}$ | 1.5 |
| $k_{\text{GDL}}$ | $1.76 \times 10^{-10}$ |
| $\varepsilon_{\text{CL}}$ | 0.4 |
| $\tau_{\text{CL}}$ | 1.5 |
| $k_{\text{CL}}$ | $1.76 \times 10^{-11}$ |
| $\varepsilon_{\text{Mem}}$ | 0.28 |
| $\tau_{\text{Mem}}$ | Dagan model |
| $k_{\text{Mem}}$ | $1.8 \times 10^{-18}$ |

general convection–diffusion equation can be expressed in conservative form as

$$\frac{\partial}{\partial t}(\rho\phi) + \nabla(\rho\vec{u}\phi - \Xi_\phi\nabla\phi) = S_\phi \quad (19)$$

where $t$ is the time, $\phi$ the general dependent variable, $\Xi_\phi$ the exchange coefficient, $S_\phi$ the source term, $\vec{u}$ the velocity vector, and $\rho$ is the density. When Eq. (20) is integrated over a control volume, the resulting finite volume equation is

$$a_P\phi_P = a_E\phi_E + a_W\phi_W + a_N\phi_N + a_S\phi_S + a_H\phi_H + a_L\phi_L + b \quad (20)$$

where $\phi_p$ is the value of variable $\phi$ at node P of the control volume, $\phi_E, \ldots, \phi_L$ the values of the variable at nodes in neighboring control volumes, $a_P, \ldots, a_L$ coefficients in the discretized equations and $b$ is the source terms for the discretized equation for $\phi$. The semi-implicit method for pressure-linked equation (SIMPLE) algorithm, developed by Patankar [38], was employed to solve the governing equations. The coupled set of equations was solved iteratively, with the solution considered to be converged when the relative error in each field between two consecutive iterations was less than $10^{-6}$. In this work, the CPU time (Intel Core 2 Duo E6300) for each case was about 20 h.

The model used non-uniformly distributed elements with 116, 93, and 33 elements in the $X$-, $Y$- and $Z$-direction (the flow channel inlets are along the $Y$-direction and the height is in the $Z$-direction). The grid independence was examined in preliminary test runs. Four non-uniformly distributed grid configurations were evaluated for the PEMFC with the parallel flow channel design. The numbers of elements in the $X$-, $Y$- and $Z$-direction were: (I) $70 \times 70 \times 25$, (II) $93 \times 93 \times 33$, (III) $116 \times 93 \times 33$, and (IV) $116 \times 116 \times 41$. The influence of the number of elements on the polarization curves ($I$–$V_{cell}$ curves) for the fuel cell is shown in Fig. 2. The polarization curve for grid (I) differs from those for grids (II–IV). At an operating voltage of 0.3 V, the deviation is about 3.9%. However, the calculated polarization curves for grids (II), (III) and (IV) do not show any notable differences. At an operating voltage of 0.3 V, the difference between the current densities for (II) and (III) is about 0.32% and the difference for (III) and (IV) is about 0.25%. Therefore, grid (III) was chosen for the simulations as a trade off between accuracy and execution time.

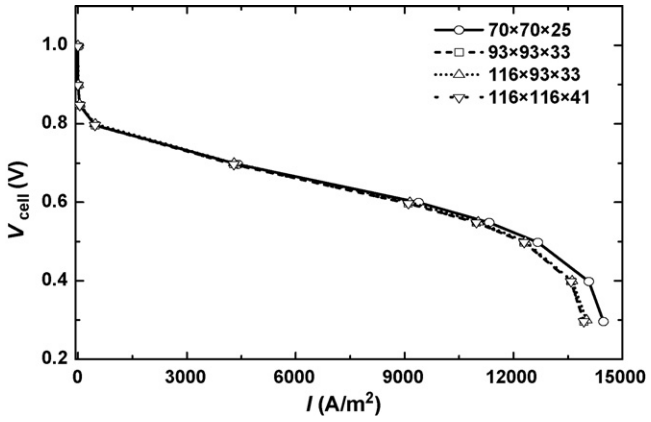


Fig. 2. Influence of the number of elements on the polarization curves.

## 4. Under-rib convection effect

When the reactants are pumped to flow through the flow channel from the inlet to the outlet, the local pressure in the channel can be approximated as [20,27–29,39]

$$P(L) = P_{in} - \frac{128\mu Q}{\pi d_{eff}^4}L \quad (21)$$

where $P_{in}$ is the inlet pressure of the reactants, $P(L)$ the local pressure of the reactants, $\mu$ the reactants viscosity, $Q$ the mass flow rate of the reactants, $d_{eff}$ the effective hydraulic diameter of the flow channel, and $L$ is distance along the channel measured from the inlet. Eq. (1) indicates that the pressure decreases with downstream due to viscous losses. For the conventional and baffled designs, each serpentine loop proceeds through three 180° turns to form 12 channels and 11 ribs. For each rib, the two channels on its left and right sides may belong to the same loop, or may belong to two different loops; therefore, the pressure differences at each location between the two channels on the left and right sides differ for the various cases. For example, for the conventional design shown in Fig. 1(a), the two channels on the left and right sides of rib 1 belong to the loops AA′ and BB′. The inlet pressures of the reactants of these two channels are almost equal; thus, the pressure difference between points a and b is nearly zero. However, the two channels on the left and right sides of rib 2 belong to the same loop, CC′; therefore, the pressure at point c is higher than that at point d. The pressure difference across the rib, i.e., between points c and d, is expressed as

$$\Delta P = \frac{128\mu Q}{\pi D_{eff}^4}(L_d - L_c) \quad (22)$$

Therefore, the pressure difference between points c and d is proportional to their distance, $L_d$–$L_c$. When the two points are near the channel inlet, the pressure difference is maximized, but is minimized near the channel bend. When the pressure gradient across the rib is much larger than the pressure gradient along the channel direction, considerable cross-leakage flow of reactants from point c to point d occurs between adjacent channels (referred to as under-rib convection [25]). According to Darcy's law, the average superficial velocity in the porous layer across the rib can be expressed as

$$v_{aver} = \frac{128k_p Q}{\pi D_{eff}^4 W_r}(L_d - L_c) \quad (23)$$

where $k_p$ is the permeability of the reactants through the GDL and $W_r$ is the rib width. Therefore, when the inlet flow rate of the reactants, the channel and rib dimensions, and permeability of the GDL remain constant, $v_{aver}$ is proportional to the distance between points c and d, $L_d$–$L_c$. Therefore, the under-rib convection is stronger near the inlet of loops CC′ and weaker at the channel bend. For the conventional design, under-rib convection also occurs under ribs 3 and 4 as well as under rib 2. The under-rib convection induces strong convection in the electrode, bringing the reactants to the CL and removing the liquid water from the reaction sites and porous electrodes, in a way

similar to the flow in the interdigitated flow channels, which results in the better overall cell performance with the serpentine flow channels. Therefore, this under-rib convection significantly influences the PEM fuel cell performance with the serpentine flow field design.

The baffles change the pressure distribution of the reactants in the channels, which will increase under-rib convection. Furthermore, near the baffles, as in the interdigitated flow field design, the reactant transport is converted to forced convection. Therefore, the baffled design is expected to enhance the reactant transport rates. For the SBFF-1 design, with the conventional design, the under-rib convection occurs under the ribs 5, 6, and 7. Moreover, because the baffles are added at the outlets of loops DD′ and FF′, the reactants still have higher pressures near the outlets of DD′ and FF′. For example, the pressures at points g and i are greater than at point h. Thus under-rib convection also occurs under ribs 8 and 9. The SBFF-2 design also has a baffle at the inlet of loop HH′; therefore, the pressures at points j and l are greater than at point k, and the pressure at point m is greater than at point n. The changes in the pressure distributions in adjacent channels results in more under-rib convection at more ribs, including ribs 10, 11, 12, 13, 14, 15, 16, and 17. Using a similar analysis for the SBFF-3, under-rib convection occurs at ribs 18, 19, 20, 21, 22, 23, 24, 25, and 26.

## 5. Results and discussions

To verify baffled design does improve cell performance, the $I$–$V_{cell}$ polarization curves and $I$–$W_{cell}$ power density curves for the conventional and baffled designs are given in Fig. 3. For operating voltages greater than 0.7 V, the conventional and baffled designs have the same performance, indicating that the cell performance is independent of the flow channel design. For operating voltages lower than 0.7 V, the cell performances of the conventional and baffled designs differ, the differences increases with the deceasing operating voltage. At the same operating voltage, the total current densities and power densities for the three baffled designs are all higher than for conventional design. The cell performance best for the SBFF-3 design, then the SBFF-2 design, the SBFF-1 design and finally the conventional design. For example, at operating voltage of 0.3 V, the total current densities for SBFF-1, SBFF-2, and SBFF-3 are 23,983, 24,882, and 25,499 A m$^{-2}$, which means that the total current densities were increased by about 10.36%, 14.50%, and 17.34% compared with the 21,731 A m$^{-2}$ for the conventional design. Thus, the baffled designs show superior performance over the conventional design.

Because the flow field designs significantly affect cell performance at low operating voltages, the local transport phenomena for the operating voltage of 0.3 V were analyzed further to understand the effect of the baffles on the cell performance. Since the power output is the consequence of the electrochemical reaction, the consumption of oxygen along the cathode GDL–CL interface is an index of the cell performance. Higher oxygen mass flow rates along the cathode GDL–CL interface means that more oxygen enters the CL to participate in the electrochemical reaction per unit time, resulting in higher current densities and better cell performance. The distributions of the oxygen mass flow rates along the cathode GDL–CL interface for the conventional and baffled designs are presented in Fig. 4. For the conventional design (Fig. 4(a)), the maximum oxygen mass flow rate occurs at the flow channel inlet and decreases along the channels forwards the outlets. Since the oxygen is gradually consumed and liquid water accumulates due to the electrochemical reaction along the flow channels. However, at the channel bends, the oxygen mass flow rate has a local peak, because the corners force oxygen flow into the GDL by forced convection. Fig. 4(a) also indicates that under ribs 2, 3, and 4, where the under-rib convection occurs, the oxygen mass flow rates are significantly higher, while under other ribs for the conventional design, the oxygen mass flow rates are very low. The higher pressure differences across ribs induce the stronger under-rib convection, so the local oxygen mass flow rates at these locations are larger. For example, for rib 4, the oxygen mass flow rates at point e are higher than at point f. Comparison of Fig. 4(a) and (b–d) shows that the oxygen mass flow rates in the baffled designs are remarkably different from that in the conventional design. The different flow rates result from two main differences between the baffled and conventional designs. First, near the baffles the oxygen transport is changed from diffusion to forced convection due to the baffle blockage effect; therefore, more oxygen enters the GDL, inducing the increased local oxygen mass flow rate. Secondly, the baffles change the reactant pressure distribution, which causes the additional under-rib convection and increases the local oxygen mass flow rates in the GDL under the ribs. For example, for SBFF-1, besides under ribs 5, 6, 7 (same locations as ribs 2, 3, and 4 for the SFF), the oxygen mass flow rates also significantly increase under ribs 8, and 9 due to the convection effects under the ribs when the flow field with baffle design is adopted. Similarly, for SBFF-2, additional the convection occurs under ribs 10, 11, 13, 16, and 17 (ribs 12, 14, and 15 have the same locations as ribs 2, 3, and 4 for the SFF), for SBFF-3, additional the convection occurs under ribs 18, 19, 21, 23, 25, and 26 (ribs 20, 22, 24 have the same locations as ribs 2, 3, and 4 for the SFF), which causes that the oxygen mass flow rates significantly increase under these ribs. Therefore, the baffled design enhances the oxygen utilization efficiency compared with the conventional design.

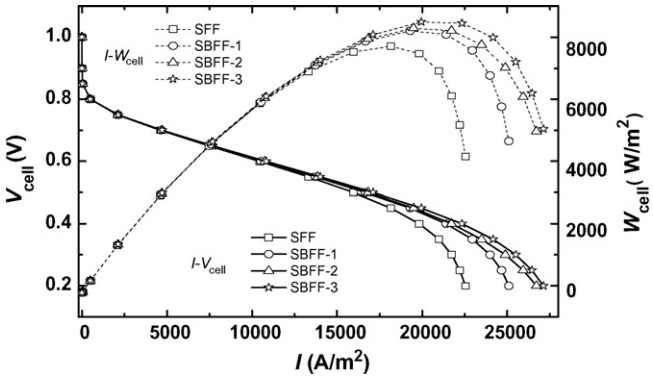


Fig. 3. Conventional and baffled cell performance characteristics.

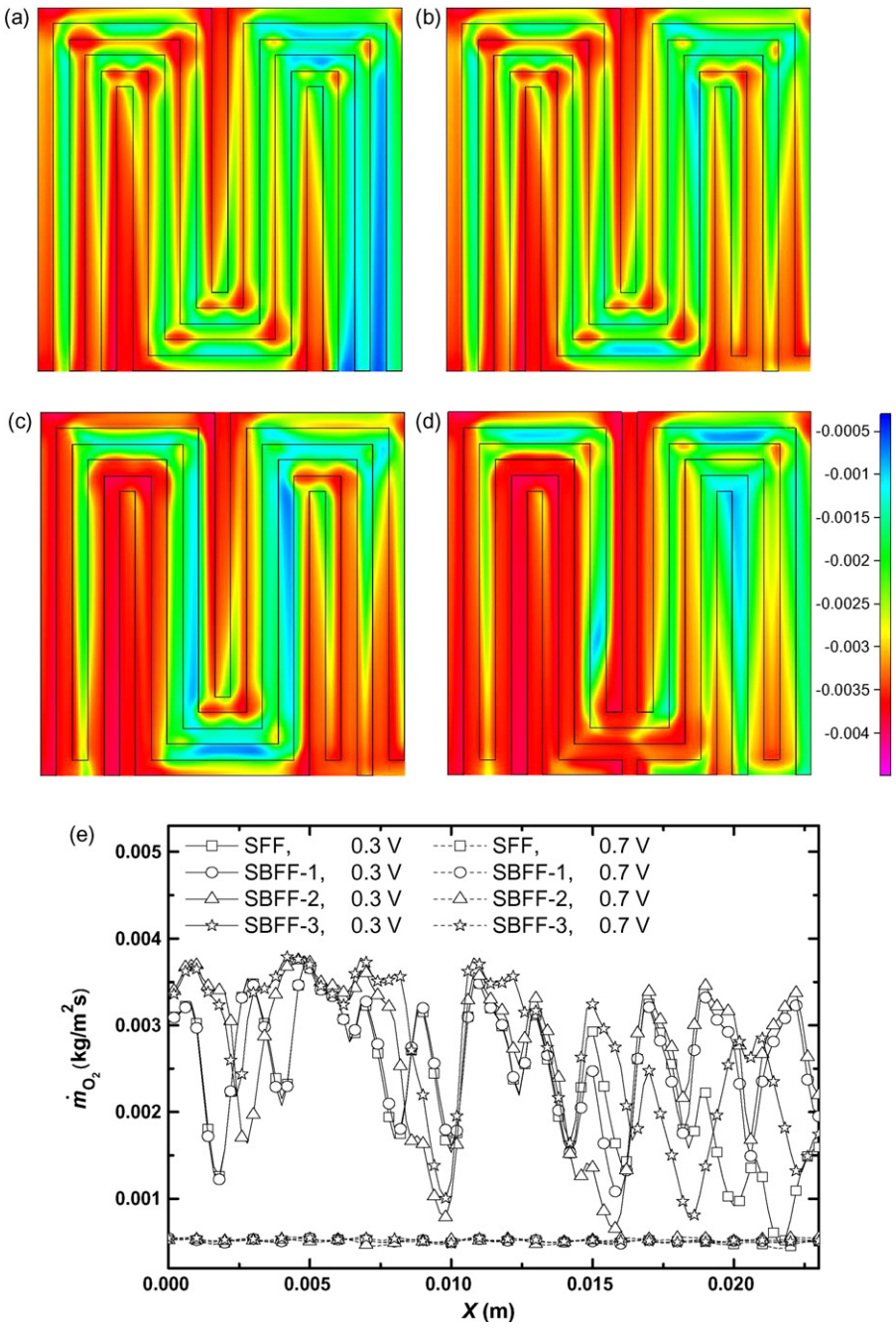


Fig. 4. Oxygen mass flow rate (kg m$^{-2}$ s) distributions on the cathode GDL–CL interface. (a) SFF; (b) SBFF-1; (c) SBFF-2; (d) SBFF-3; and (e) $y = 11.5$ mm.

The oxygen mass flow rate also significantly affects the liquid water distribution. High oxygen mass flow rates mean that more oxygen enters the CL per unit time to participate in the electrochemical reaction and more liquid water is produced. On the other hand, high oxygen mass flow rates also induce large shear forces which more efficiently remove the liquid water. Fig. 5 shows the liquid water distributions on the cathode GDL–CL interface for the conventional and baffled designs. Comparison of Figs. 5 and 4 shows that the liquid water distributions are opposite to the oxygen mass flow rate distributions, indicating that increasing the oxygen mass flow rate tends to promote liquid water removal. Liquid management is very important for improving PEMFC performance. If the liquid water produced by the electrochemical reaction is not removed, it will accumulate in the pores of the porous layer which significantly increases the oxygen transport resistance and decreases the electrochemical reaction rate. The cell performance sharply decreases when flooding occurs. Thus, appropriate flow field designs can enhance the reactant transport rate and the liquid water removal rate, as a result, the mass limitations are reduced and cell performance improves. Fig. 5 shows that the baffled designs have higher oxygen mass transport rates and liquid water removal efficiencies than the conventional design; therefore, the liquid water content in the porous layers is significantly reduced.

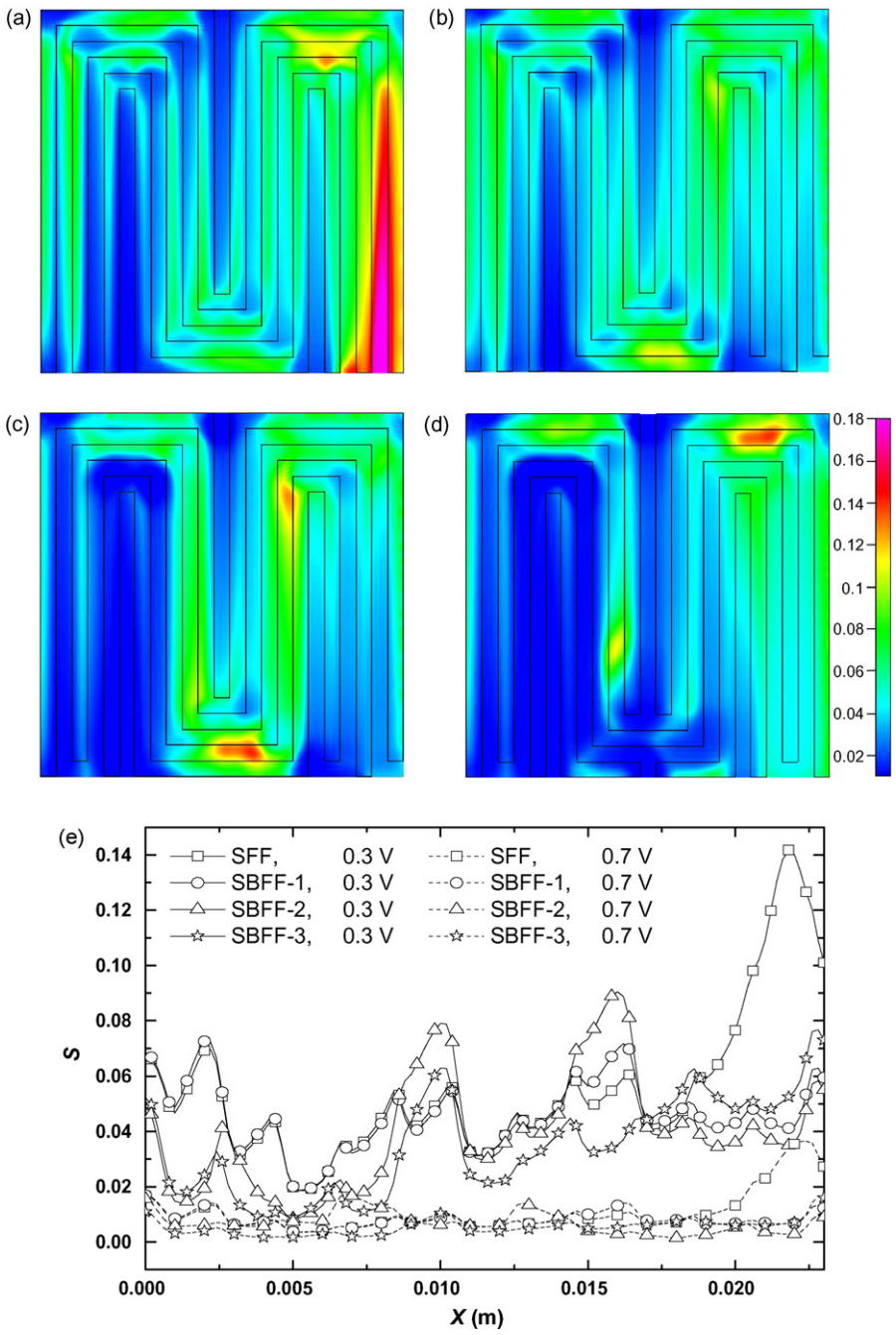


Fig. 5. Liquid water distributions on the cathode GDL–CL interface. (a) SFF; (b) SBFF-1; (c) SBFF-2; (d) SBFF-3; and (e) $y = 11.5$ mm.

Fig. 6 presents the local current densities on the middle cross-section in the PEM for the conventional and baffled designs. The oxygen consumption rates determine the power output; thus, a high oxygen mass flow rate corresponds to a high local current density. Comparison of Figs. 6 and 4 shows that the distributions of the local current densities are similar to those of the oxygen mass flow rates, confirming the accuracy of the model. Figs. 4–6 indicate that with the baffles, the baffled designs significantly improve the oxygen utilizations, by producing higher oxygen mass flow rates and lower liquid water distributions in the porous layers; therefore, the cell performance significantly improves. Because the baffles are added at different locations in the channels, the strength and extent of the additional under-rib convection between adjacent channels and the forced convection near the baffles differ for the three baffled designs, resulting in different cell performance characteristics for SBFF-1, SBFF-2, and SBFF-3. On the whole, the performance of SBFF-3 is better than that of SBFF-2, which is better than that of SBFF-1.

The flow field design influences not only the cell performance but also the pressure drop in the fuel cell. Larger pressure drops in the fuel cell mean that more power is needed to pump the reactants. Thus, the pressure drop is a significant issue to be considered in choosing the flow field designs in addition to the $I$–$V_{cell}$ curve. Figs. 7 and 8 present, respectively, the pressure

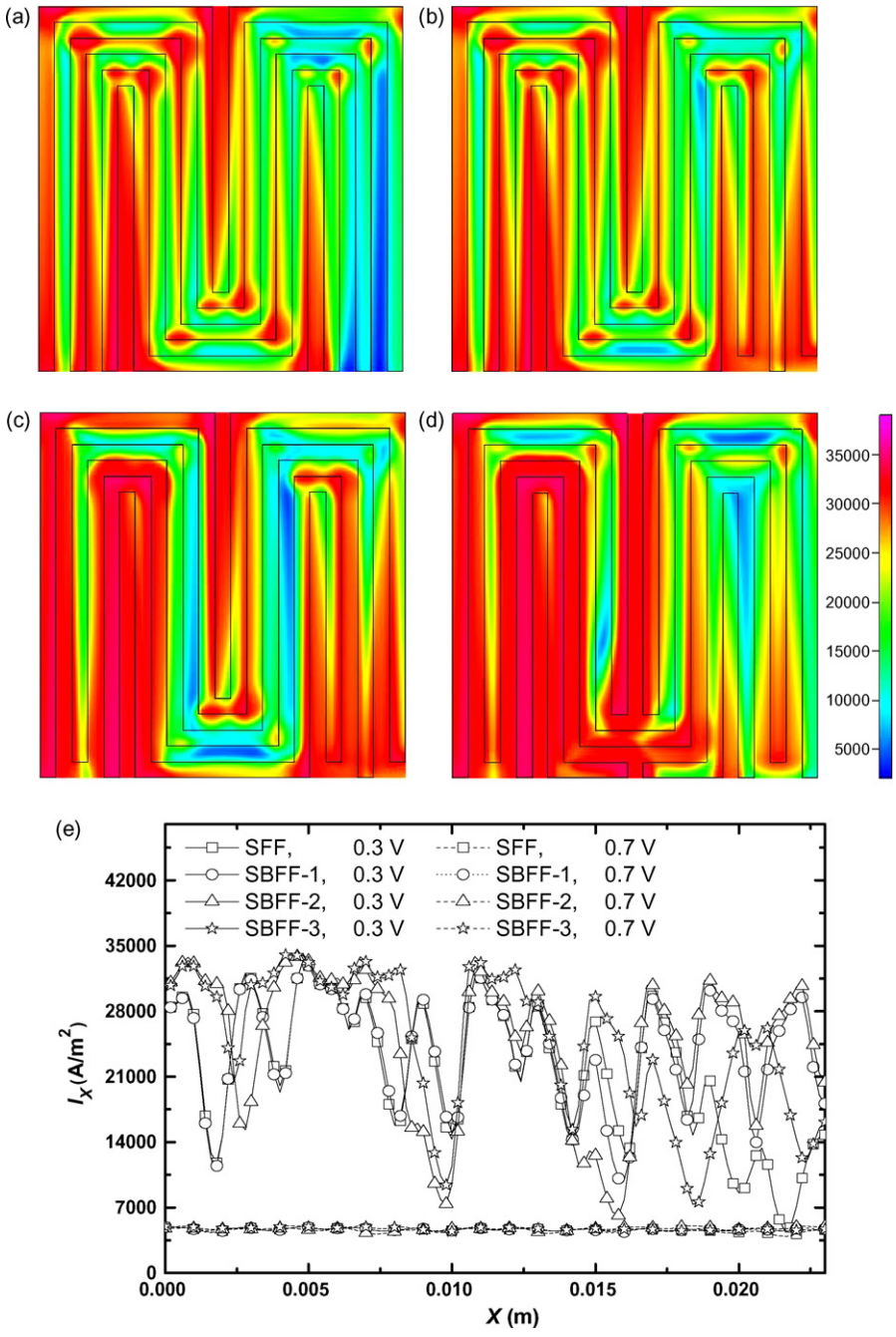


Fig. 6. Current density distributions (A m$^{-2}$) on the middle cross-section in the PEM. (a) SFF; (b) SBFF-1; (c) SBFF-2; (d) SBFF-3; and (e) $y = 11.5$ mm.

distributions on the middle cross-section in the cathode flow channels and the total pressure drops on the cathode side for the conventional and baffled designs. The total pressure drops are, respectively, 608, 1204, 817, and 692 Pa for SFF, SBFF-1, SBFF-2, and SBFF-3. It indicates that the pressure drops for baffled designs are higher than that for the conventional design. The cathode pressure drop is related to the power density by [21]:

$$W_P = \frac{\Delta P A_{\text{cha}} V}{A_{\text{total}}} \tag{24}$$

where $W_P$, represents the cathode pressure drop loss, $\Delta P$ the total cathode pressure drop across the fuel cell, $A_{\text{cha}}$ the cathode cross-sectional inlet flow area, $V$ the fuel velocity at the cathode inlet, and $A_{\text{total}}$ is the reaction area. The calculated cathode pressure drop losses and output power for the conventional and baffled designs are listed in Table 4. Although the pressure drops for the baffled designs are larger than for the conventional design, the pressure drop losses are far less than the cell output power for the miniature fuel cells analyzed here. Thus, the pressure drop losses can be ignored.

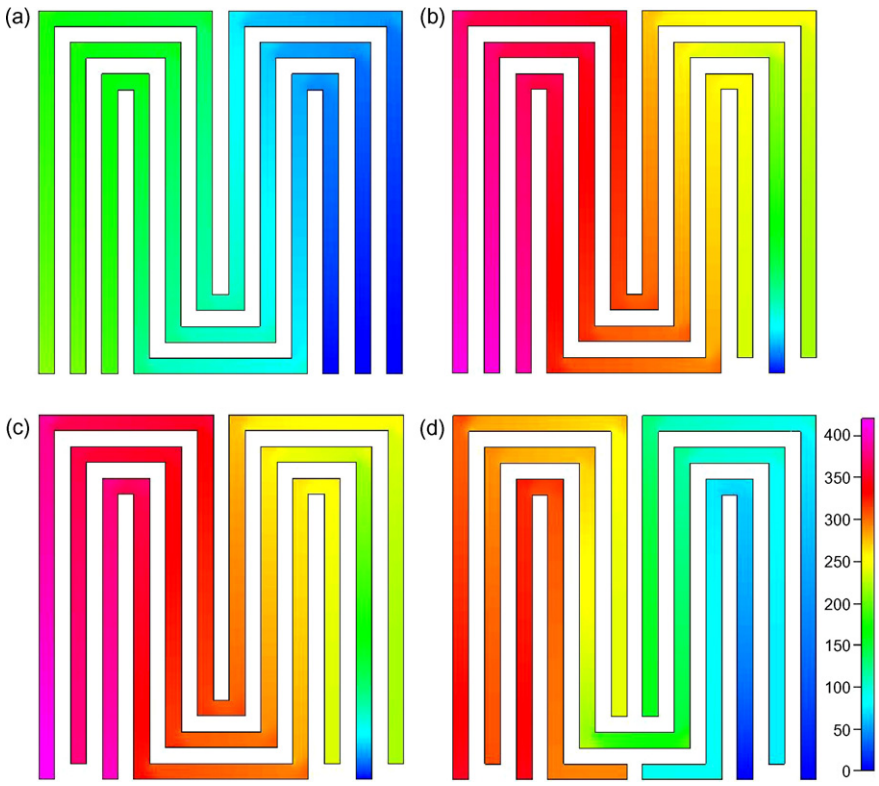


Fig. 7. Pressure distributions (Pa) on the middle cross-section in the cathode channels. (a) SFF; (b) SBFF-1; (c) SBFF-2; and (d) SBFF-3.

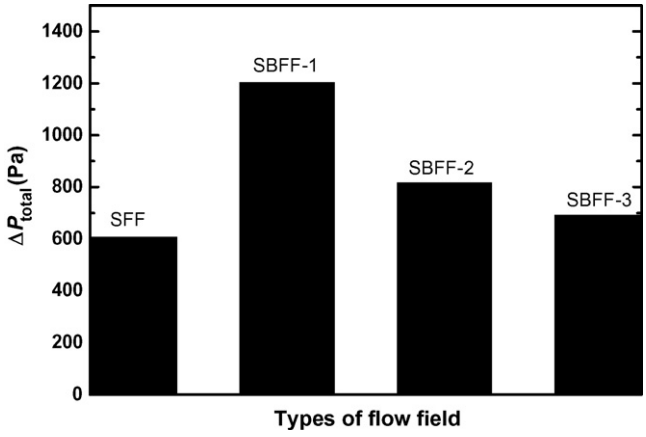


Fig. 8. Total pressure drops on the cathode side for the conventional and baffled designs.

Table 4
Estimation of pressure drop losses at the operating voltage of 0.3 V

| Flow field type | $\Delta p$ (Pa) | $W_{cell}$ (W m$^{-2}$) | $W_p$ (W m$^{-2}$) | $W_{net}$ (W m$^{-2}$) |
|---|---|---|---|---|
| SFF | 608 | 6518.96 | 4.47 | 6515.49 |
| SBFF-1 | 1204 | 7194.98 | 8.85 | 7186.13 |
| SBFF-2 | 817 | 7464.65 | 9.01 | 7455.64 |
| SBFF-3 | 692 | 7649.92 | 7.63 | 7642.29 |

## 6. Conclusions

An appropriate design of the flow channels in the bipolar plates can significantly impact the thermal and water management of the PEMFC. A novel baffled design is presented here to provide the significantly better performance than the conventional design. A three-dimensional numerical model is used to predict the local transport phenomena and cell performance for the baffled and conventional designs. The conclusions drawn from the analyses are

1. The analysis shows that the effect of the baffles on cell performance is dependent on the operating conditions. At high operating voltages, the flow field design has little effect on cell performance because the electrochemical reaction rate is low and only a limited amount of oxygen is consumed with only a small amount of liquid water produced. Therefore, the oxygen transport rates for both the baffled and conventional designs are sufficient to maintain the reaction rates.
2. At low operating voltages, the cell performance is strongly dependent on the flow field design. Compared with the conventional design, the baffled design significantly enhances the mass transport capability and the efficiency of liquid water removal, which results in better performance than with the conventional design. The baffles in the channels on the cathode side force the reactants near the baffles into the GDL and CL to enhance the electrochemical reaction rate at the CL. The baffles also increase the reactant pressure in the channels; thus, the under-rib convection occurs under more ribs, which increases the reactant mass flow rate under those ribs.
3. For the miniature PEMFC analyzed here, the compressor power needed to overcome the cell pressure drop is far less than the cell output power and can be neglected; thus, the baf-

fled design has superior performance over the conventional design.

## Acknowledgment

This study was supported by the National Natural Science Foundation of China (Grant No. 50636020).

## References

[1] J. Larmine, A. Dicks, Fuel Cell Systems Explained, 2nd ed., Wiley, Chichester, West Sussex, 2003.
[2] H. Yang, T.S. Zhao, Q. Ye, J. Power Sources 139 (2005) 79.
[3] X.G. Li, I. Sabir, J. Hydrogen Energy 30 (2005) 359.
[4] M.M. Mench, Q.L. Dong, C.Y. Wang, J. Power Sources 124 (2003) 90.
[5] S.H. Ge, X.G. Li, I.M. Hsing, J. Electrochem. Soc. 151 (2004) B523.
[6] G.Q. Lu, C.Y. Wang, J. Power Sources 134 (2004) 33.
[7] R. Satija, D.L. Jacobson, M. Arif, S.A. Werner, J. Power Sources 129 (2004) 238.
[8] U. Pasaogullari, C.Y. Wang, J. Electrochem. Soc. 151 (2004) A399.
[9] Q. Dong, J. Kull, M.M. Mench, J. Power Sources 139 (2005) 106.
[10] H. Meng, C.Y. Wang, J. Electrochem. Soc. 152 (2005) A1733.
[11] G. Lin, T.V. Nguyen, J. Electrochem. Soc. 152 (2005) A1942.
[12] H. Yamada, T. Hatanaka, H. Murata, Y. Morimoto, J. Electrochem. Soc. 153 (2006) A1748.
[13] A. Turhan, K. Heller, J.S. Brenizer, M.M. Mench, J. Power Sources 160 (2006) 1195.
[14] F.B. Weng, A. Su, C.Y. Hsu, C.Y. Lee, J. Power Sources 157 (2006) 674.
[15] J. Scholta, F. Häussler, W. Zhang, L. Kuppers, L. Jörissen, W. Lehnert, J. Power Sources 155 (2006) 60.
[16] Y. Wang, C.Y. Wang, J. Power Sources 153 (2006) 130.
[17] L. Sun, P.H. Oosthuizen, K.B. McAuley, Int. J. Therm. Sci. 45 (2006) 1021.
[18] S.S. Hsieh, S.H. Yang, C.L. Feng, J. Power Sources 162 (2006) 262.
[19] J.H. Jang, W.M. Yan, H.Y. Li, Y.C. Chou, J. Power Sources 159 (2006) 468.
[20] J.P. Feser, A.K. Prasad, S.G. Advani, J. Power Sources 161 (2006) 404.
[21] S.W. Cha, R.O. Hayre, Y. Saito, F.B. Prinz, J. Power Sources 124 (2004) 57.
[22] W.M. Yan, H.Y. Hung, W.C. Tsai, J. Electrochem. Soc. 153 (2006) A1984.
[23] X.D. Wang, Y.Y. Duan, W.M. Yan, J. Power Sources 172 (2007) 265.
[24] T.V. Nguyen, J. Electrochem. Soc. 143 (1996) L103.
[25] C. Xu, T.S. Zhao, Electrochem. Commun. 9 (2007) 497.
[26] S.W. Cha, R. O'Hayre, S.J. Lee, Y. Saito, F.B. Prinz, J. Electrochem. Soc. 151 (2004) 1856.
[27] M.V. Williams, H.R. Kunz, J.M. Fenton, J. Electrochem. Soc. 151 (2004) A1617.
[28] C. Xu, Y.L. He, T.S. Zhao, R. Chen, Q. Ye, J. Electrochem. Soc. 153 (2006) A1358.
[29] Q. Ye, T.S. Zhao, C. Xu, Electrochim. Acta 51 (2006) 5420.
[30] W.M. Yan, C.Y. Soong, F.L. Chen, H.S. Chu, J. Power Sources 143 (2005) 48.
[31] C.Y. Soong, W.M. Yan, C.Y. Tseng, H.C. Liu, F.L. Chen, H.S. Chu, J. Power Sources 143 (2005) 36.
[32] H.C. Liu, W.M. Yan, C.Y. Soong, F.L. Chen, J. Power Sources 142 (2005) 125.
[33] H.C. Liu, W.M. Yan, C.Y. Soong, F.L. Chen, H.S. Chu, J. Power Sources 158 (2006) 78.
[34] W. He, J.S. Yi, T.V. Nguyen, AIChE J. 46 (2000) 2053.
[35] S. Mazumder, J.V. Cole, J. Electrochem. Soc. 150 (2003) A1503.
[36] V. Gurau, H. Liu, S. Kakac, AIChE J. 44 (1998) 2410.
[37] T.E. Springer, T.A. Zawodizinski, S. Gottesfeld, J. Electrochem. Soc. 138 (1991) A2334.
[38] S.V. Patankar, Numerical Heat Transfer and Fluid Flow, Hemisphere/McGraw-Hill, New York, 1980.
[39] T. Kanezaki, X. Li, J.J. Baschuk, J. Power Sources 162 (2006) 415.